Development of a GOES-R Advanced Baseline Imager Solar Channel Radiance Simulator for Ice Clouds

SHOUGUO DING AND PING YANG

Department of Atmospheric Sciences, Texas A&M University, College Station, Texas

BRYAN A. BAUM

Space Science and Engineering Center, University of Wisconsin—Madison, Madison, Wisconsin

ANDREW HEIDINGER

NOAA/NESDIS/Center for Satellite Applications and Research, Madison, Wisconsin

THOMAS GREENWALD

Space Science and Engineering Center, University of Wisconsin—Madison, Madison, Wisconsin

(Manuscript received 26 June 2012, in final form 24 October 2012)

ABSTRACT

This paper describes the development of an ice cloud radiance simulator for the anticipated Geostationary Operational Environmental Satellite R (GOES-R) Advanced Baseline Imager (ABI) solar channels. The simulator is based on the discrete ordinates radiative transfer (DISORT) model. A set of correlated *k*-distribution (CKD) models is developed for the ABI solar channels to account for atmospheric trace gas absorption. The CKD models are based on the ABI spectral response functions and also consider when multiple gases have overlapping absorption. The related errors of the transmittance profile are estimated on the basis of the exact line-by-line results, and it is found that errors in transmittance are less than 0.2% for all but one of the ABI solar channels. The exception is for the 1.378-μm channel, centered near a strong water vapor absorption band, for which the errors are less than 2%. For ice clouds, the band-averaged bulk-scattering properties for each ABI [and corresponding Moderate Resolution Imaging Spectroradiometer (MODIS)] solar channel are derived using an updated single-scattering property database of both smooth and severely roughened ice particles, which include droxtals, hexagonal plates, hexagonal hollow and solid columns, three-dimensional hollow and solid bullet rosettes, and several types of aggregates. The comparison shows close agreement between the radiance simulator and the benchmark model, the line-by-line radiative transfer model (LBLRTM)+DISORT model. The radiances of the ABI and corresponding MODIS measurements are compared. The results show that the radiance differences between the ABI and MODIS channels under ice cloud conditions are likely due to the different band-averaged imaginary indices of refraction.

1. Introduction

The Advanced Baseline Imager (ABI) will be on the Geostationary Operational Environmental Satellite (GOES) R series (Schmit et al. 2005) and is scheduled to launch in 2015. The ABI will have a higher spatial resolution and more spectral bands than the previous GOES imagers. The 16 spectral channels include 2 visible (VIS) channels, 4 shortwave infrared (SWIR) channels, and 10 infrared (IR) channels. To infer cloud properties from the ABI solar channels (VIS and SWIR), an accurate forward radiative transfer model (RTM) would be invaluable for generating simulated radiances and fluxes for a variety of atmospheric and surface conditions. An accurate RTM can also be used for error analyses and instrument calibration efforts.

In this paper, our goal is to develop an ABI radiance simulator to simulate ice cloud radiances for the solar bands. A set of correlated *k*-distribution (CKD) models

Corresponding author address: Prof. Ping Yang, Dept. of Atmospheric Sciences, Texas A&M University, College Station, TX 77843.
E-mail: pyang@tamu.edu

DOI: 10.1175/JAMC-D-12-0180.1

© 2013 American Meteorological Society

is developed for the ABI solar channels to account for gaseous absorption in the atmosphere. Consideration of both the instrument spectral response functions and gas absorption (including overlapping gas absorption) is included in the CKD models and incorporated into the RTM. The ABI radiance simulator is developed by combining the CKD model with the well-known discrete ordinate radiative transfer (DISORT) model to handle the gaseous absorption and multiple scattering due to the ice cloud particles. Comparisons of radiances simulated from the simulator and a reference model, the line-by-line radiative transfer model (LBLRTM)+DISORT model (Ding et al. 2011), are made for the purpose of validation.

For the ABI solar bands, ice cloud bulk scattering models are developed for each channel using the updated single-scattering property database of nonspherical ice particles, which include droxtals, hexagonal plates, hexagonal hollow and solid columns, three-dimensional hollow and solid bullet rosettes, and several types of aggregates based on columns or plates. Bulk scattering models are developed for a set of particles with smooth surfaces and also severe surface roughening (Baum et al. 2011).

The resulting simulator is tested to investigate the differences between the radiances anticipated from the ABI solar channels and those measured from corresponding MODIS channels. For use in the simulated radiance comparison, profiles of atmospheric absorption optical thickness are generated from the CKD models using Modern Era Retrospective Analysis for Research and Applications (MERRA) products (Bosilovich et al. 2011; Rienecker et al. 2011). The optical thickness and the effective particle size are obtained from the operational Collection 5 Moderate Resolution Imaging Spectroradiometer (MODIS) cloud product. Based on the MODIS ice cloud optical thickness and effective particle size as model inputs, the ice cloud reflectances of individual ABI solar channels are simulated and compared with collocated MODIS measurements.

The paper is organized as follows. Section 2 describes the development of the CKD method. Section 3 briefly describes the single-scattering properties of the ice particles and the development of the bulk scattering properties of ice clouds. Section 4 describes the establishment of the ABI solar ice cloud radiance simulator. In section 5, the simulator is exercised using the collocated MERRA atmospheric profiles and retrieved effective particle size and optical thickness as inputs, and the resulting radiances are compared with those measured from the MODIS granule. A summary is given in section 6.

2. Development of the CKD model

The CKD method is an excellent approximation to the line-by-line radiative transfer model and has noted advantages over the conventional band models (Edwards and Francis 2000; Fu and Liou 1992; Goody and Yung 1989; Kratz 1995; Lacis and Oinas 1991; Li and Barker 2005; Shi 1984; Zhang et al. 2003) since it can account for nongray gaseous absorption and be readily incorporated into multiple scattering RTMs for aerosol and cloud calculations. For the CKD models developed in this study for the ABI solar channels, the absorption coefficients for the gases of interest are based on the LBLRTM (Clough et al. 2005). The molecular absorption line parameters used for absorption coefficient calculations are based on the 2008 edition of the High Resolution Transmission (HITRAN) molecular spectroscopic database (Rothman et al. 2009), with the exception of the ozone absorption coefficients in the visible wavelength range that are based on the World Meteorological Organization/International Ozone Commission (Burrows et al. 1999; Orphal 2003).

a. CKD method for remote sensing applications

The ABI spectral response function of each ABI solar channel is considered. An approximate method (Kratz 1995; Kratz and Rose 1999) divides the spectral interval of interest into subintervals, and in each subinterval the instrument response is considered to be constant. Since the spectral response functions of many instruments are broad enough so that a channel can have complex absorption features, Greenwald and Drummond (1999) took into consideration the spectral response function across the full band by using the mean response function over each quadrature weight within the context of the CKD model. Edwards and Francis (2000) suggested a different approach to including the instrument spectral response function during the derivation of the CKD model. In this study, we follow the approach of Edwards and Francis (2000). In their approach, the band transmittance for each atmospheric layer is given by

$$\Gamma_\phi = \frac{1}{F_\phi}\int_{\Delta\nu} t(\nu)\phi(\nu)\,d\nu, \tag{1}$$

where ν is the wavenumber, $t(\nu)$ is the monochromatic transmittance, $\phi(\nu)$ is the instrument spectral response function, and the integrated spectral response is given by

$$F_\phi = \int_{\Delta\nu} \phi(\nu)\,d\nu. \tag{2}$$

Consider a spectral channel with interval $\Delta\nu$ that contains numerous absorption lines for which the interval is divided into M subintervals of width $\delta\nu_m$ $(1 \le m \le M)$.

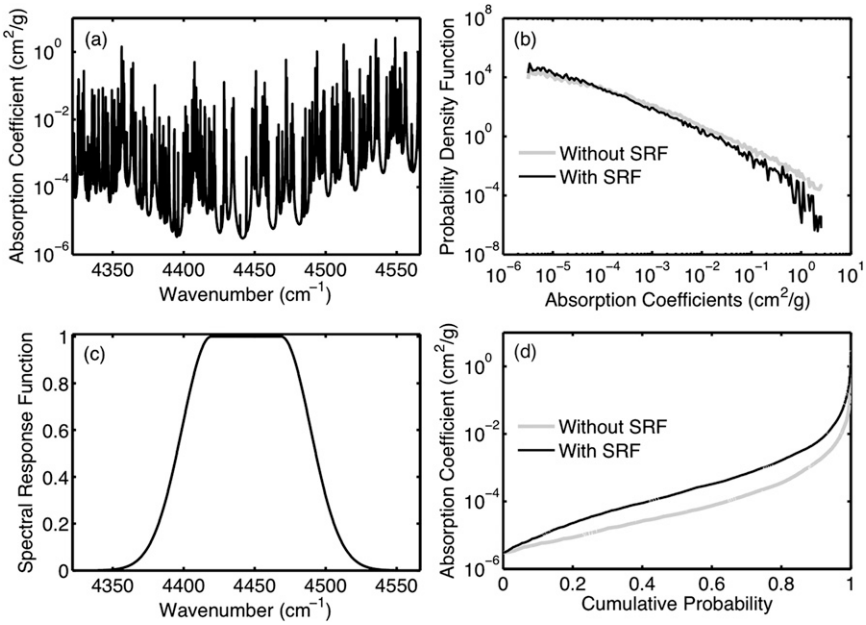

FIG. 1. Application of the CKD method to water vapor absorption for the ABI 2.25-μm NIR channel. (a) Absorption coefficient k (cm^2 g^{-1}) as a function of wavenumber at the reference conditions of 260 K and 398 hPa. (b) Probability density function of the absorption coefficients, including the instrument response. (c) The instrument spectral response function of the ABI 2.25-μm channel. (d) The absorption coefficient as a function of the cumulative probability.

The corresponding instrument response is ϕ_m. The range of the absorption coefficient $k(\nu)$ is divided into $n = 1 - N$ subintervals with specified width δk_n and $k_n = k_{n-1} + \delta k_n$. The probability density function can be written as

$$f_\phi(k_n) = \frac{1}{F_\phi} \sum_{m=1}^{M} \left| \frac{\phi_m \delta \nu_m}{\delta k_n} \right| W_m \quad (k_n \le k_m \le k_{n+1}), \quad (3)$$

where W_m is the window function associated with the mth subinterval, defined by

$$W_m = \begin{cases} 1, & k_n \le k_m \le k_{n+1} \\ 0, & \text{otherwise} \end{cases}. \quad (4)$$

The corresponding cumulative distribution function $g_\phi(k)$ can be calculated as

$$g_\phi(k_n) = \frac{1}{F_\phi} \sum_{m=1}^{M} \phi_m \delta \nu_m W_m \quad (k_{n-1} \le k_m \le k_n). \quad (5)$$

By definition, $g_\phi(k_n)$ is a monotonically increasing and smooth function of k, ranging from 0 to 1. The inverse, $k_\phi(g_n)$, is referred to as the k distribution. In this way, the instrument spectral response function is included in the k distribution. Based on the method described above, we developed a set of CKD models for the ABI solar channels. Figure 1 illustrates the process through which the absorption coefficients are transformed from a rapidly oscillating function of wavenumber to a smooth function of g. Note that many fewer quadrature points are necessary to calculate the spectral transmittance in g space than in wavenumber space. Figure 1a shows the mass absorption coefficients (cm^2 g^{-1}) associated with water vapor between 4321.55 and 4566.55 cm^{-1} for a pressure of 398 hPa and a temperature of 260 K. Figure 1b shows the probability density distributions for the absorption coefficients. Figure 1c is the spectral response function of the GOES-R ABI 2.25-μm near-infrared (NIR) channel, which is based on the University of Wisconsin ABI spectral response function (downloaded from ftp://ftp.ssec.wisc.edu/ABI/SRF). Figure 1d shows the absorption coefficient as a function of cumulative probability g. For comparison, the probability density function and cumulative probability calculated without considering the instrument spectral response function are provided as the gray lines in Figs. 1b and 1d, respectively. It is evident that the spectral response function can have a significant impact on the probability density function and thus the k distributions.

b. The gaseous overlapping absorption in the CKD method

The treatment of overlapping absorption lines presents a key issue for most radiative transfer models and also for the derivation of the CKD model. Generally, it is assumed that gas absorption is independent between species so that the absorption coefficients are uncorrelated. The spectral mean transmittance of two overlapping gases for a given band can be calculated based on the multiplication property (Goody and Yung 1989) given by the following relationship:

$$\begin{aligned}\Gamma_{\Delta\nu}(1,2) &= \Gamma_{\Delta\nu}(1)\times\Gamma_{\Delta\nu}(2)\\ &= \sum_{i=1}^{M}\exp(-k_{1,i}u_1)\Delta g_{1,i}\sum_{j=1}^{N}\exp(-k_{2j}u_2)\Delta g_{2,j}\\ &= \sum_{i=1}^{M}\Delta g_{1,i}\sum_{j=1}^{N}\Delta g_{2,j}\exp(-k_{1,i}u_1-k_{2j}u_2),\end{aligned} \tag{6}$$

where $\Gamma_{\Delta\nu}(1, 2)$ is the total transmittance of the band; $\Gamma_{\Delta\nu}(1)$ and $\Gamma_{\Delta\nu}(2)$ are the transmittances due to absorbing gases 1 and 2, respectively; and u_1 and u_2 are the absorber amounts of the two overlapping gases 1 and 2. In addition, M and N are the total numbers of g values for two gases. Based on Eq. (6), a total of $M \times N$ calculations are required to obtain the spectral mean transmittance in a spectral interval $\Delta\nu$ where the two gases overlap. This method can also be applied to bands with three or more overlapping gases. However, the number of calculations will increase for each additional absorbing gas. Although this approach produces accurate results, the method tends to be computationally inefficient (Lacis and Oinas 1991).

An alternative approach is referred to as the modified amount weighted scheme (Fu and Liou 1992; Li and Barker 2005; Shi et al. 2009). The idea is to treat the gaseous mixture as a "single gas" by combining the absorption coefficients of the mixture of all absorption gases. The absorption coefficients are weighted by absorber amounts. Following Shi et al. (2009), the total optical thickness can be given by

$$\begin{aligned}\tau(\nu) &= \tau_1(\nu)+\tau_2(\nu)+\cdots+\tau_n(\nu)\\ &= \sum_l[k_1(\nu)u_1+k_2(\nu)u_2+\cdots+k_n(\nu)u_n];\end{aligned} \tag{7}$$

choosing the dominant gas 1, Eq. (7) can change to

$$\begin{aligned}\tau(\nu) &= \sum_l u_1\left[k_1(\nu)+k_2(\nu)\frac{u_2}{u_1}+\cdots+k_n(\nu)\frac{u_n}{u_1}\right]\\ &= \sum_l u_1[k_1(\nu)+r_2k_2(\nu)+\cdots+r_nk_n(\nu)]\\ &= \sum_l u_1k_{\mathrm{comb}}(\nu),\end{aligned} \tag{8}$$

where $k_{\mathrm{comb}}(\nu) = k_1(\nu) + r_2k_2(\nu) + \cdots + r_nk_n(\nu)$ can be considered to be the absorption coefficient for a single-mixture gas. The dominant gas is regarded to as the reference gas. As indicated by Shi et al. (2009), the distribution of combined absorption coefficients will generally reflect the spectral features of the principal contributor. Through Eq. (8), overlapping absorption by multiple gases is converted into a single-gas case. Fu and Liou (1992) pointed out that the same assumptions regarding the correlations for each individual gas are required for the single-gaseous mixture. Under such an assumption, the single-mixture gas can be efficiently handled by the CKD method. In this study, we followed this approach to treat the gaseous overlapping absorptions during the derivation of the CKD model.

Figure 2 shows an example of the treatment of overlap absorption bands based on the k distribution for the ABI 1.61-μm SWIR channel. Figures 2a–c show the absorption coefficients as a function of wavenumber for H_2O, CO_2, and CH_4, respectively. Figure 2d shows the mixed gas in the ABI 1.61-μm channel. Figure 2e is the spectral response function and Fig. 2f shows the absorption coefficient as a function of the cumulative probability for the single-mixture gas with the spectral response function included.

c. Construction of the CKD models for the ABI solar channels

We now describe the construction of the CKD model for the ABI solar channels, based on the theory and techniques described in the previous sections. To use the k distribution method for a realistic atmosphere, we must extend it to inhomogeneous profiles. At different pressures and temperatures, the k distributions are assumed to be correlated with those at the reference pressure and temperature and thus for all atmospheric conditions. This means that each of the sets of absorption coefficients calculated with the line-by-line model can then be sorted and binned with the same distribution as that of the reference pressure and temperature. For the present study, the absorption coefficients were calculated for 19 pressures with $\Delta\log_{10}P = 0.2$ along with three temperatures, 200, 260, and 320 K, which cover most atmospheric conditions.

The absorption coefficients at arbitrary pressures and temperatures are calculated by following Chou and Kouvaris (1986):

$$\ln[k(\nu,p,T)] = a(\nu,p)(T-260)+c(\nu,p)(T-260)^2, \tag{9}$$

where the coefficients a, b, and c are calculated at 200, 260, and 320 K. Since the cumulative probability g is

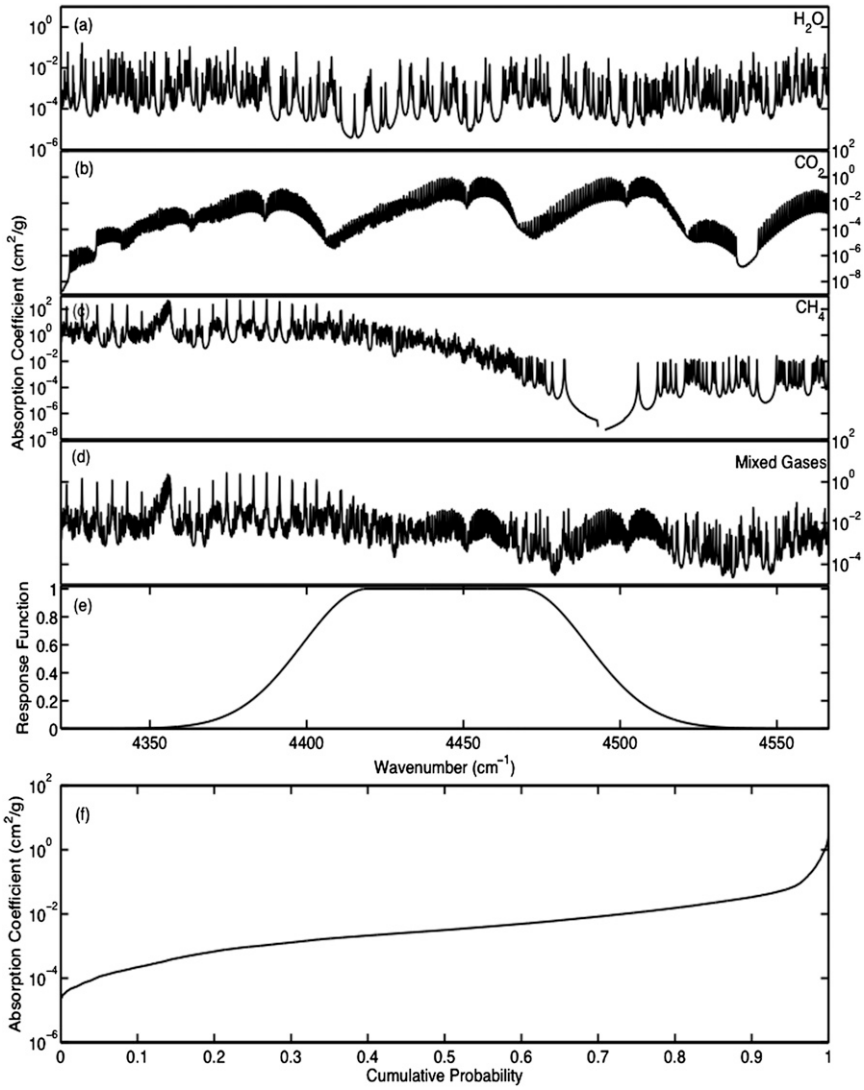

FIG. 2. Example of the treatment of overlap absorption bands based on the k distribution for the ABI 1.61-μm channel. Absorption coefficient as a function of wavenumber for (a) H_2O, (b) CO_2, (c) CH_4, and (d) mixed gases in the ABI 1.61-μm channel. (e) Spectral response function. (f) Absorption coefficient as a function of cumulative probability for the single gas mixture with the spectral response function included.

derived to be equivalent to the wavenumber, Eq. (9) can also be applied for a given g (Fu and Liou 1992):

$$\ln[k(g,p,T)] = a(g,p) + b(g,p)(T-260) + c(g,p)(T-260)^2, \quad (10)$$

where, $a(g, p)$, $b(g, p)$, and $c(g, p)$ are regression coefficients that are determined from the g values at 19 pressures and three temperatures. The coefficients $a(g, p)$, $b(g, p)$, and $c(g, p)$ are stored at each g and pressure. The $k(g, p, T)$ at an arbitrary pressure is obtained by linear interpolation between values at two neighboring pressures.

In most RT calculations of cloudy-sky conditions, only water vapor and ozone concentration profiles are considered to change with time and space, while other trace gases are assumed to have constant mixing ratios at each layer. In the present study, the atmosphere is assumed to be uniformly mixed for O_2, CO_2, CH_4, and N_2O with volume mixing ratios of 0.209 48, 3.80×10^{-4}, 1.774×10^{-6}, and 3.19×10^{-7} (Solomon et al. 2007), respectively. As noted previously, the CKD model is based on 19 pressures and three temperatures. For

TABLE 1. Summary of the wavelengths and absorbers of the ABI solar channels.

ABI channel	Spectral range (μm)	Central wavelength (μm)	Absorbers
1	0.45–0.49	0.47	O_3 and H_2O
2	0.59–0.69	0.64	O_3 and H_2O
3	0.846–0.885	0.865	H_2O, O_2, and CO_2
4	1.371–1.386	1.378	H_2O, CO_2, and CH_4
5	1.58–1.64	1.61	H_2O, CH_4, and CO_2
6	2.225–2.275	2.25	H_2O, CH_4, NO_2, and CO_2

ABI channels 1 and 2 (centered at 0.47 and 0.64 μm, respectively), absorption coefficients of O_3 are considered to be independent of temperature and pressure (Orphal 2003). In the SWIR range, all radiatively active gases are considered together as a single fixed gas in the CKD models. The species of absorber included in the fixed gas depends on the ABI channel, as shown in Table 1.

We now examine the related errors of the transmittance profile based on the exact line-by-line results. Panels in the left column of Fig. 3 show the comparisons of ABI band-averaged transmittances simulated from the CKD models and the LBLRTM. Panels in the right column are the corresponding relative error profiles of the CKD models. The standard tropical atmospheric profile is used in the calculations. It can be seen clearly from Fig. 3 that relative errors in transmittance are less than 0.2% for most ABI solar channels, except for the ABI 1.378-μm channel, which is located in the strong water vapor absorption band. The errors in the ABI 1.378-μm channel are still under 2%.

3. Bulk optical properties of ice clouds

Two different sets of bulk ice cloud scattering–absorption properties are used in this paper.

a. Ice particle models based on smooth surfaces

The first set of models is developed with the same assumptions adopted for the MODIS lookup tables (LUTs) used for operational MODIS Collection 5 processing. The models were redeveloped for this study using the updated single-scattering libraries described in Baum et al. (2011). The ice particles are assumed to have smooth surfaces except for the aggregate of columns, which is severely roughened. For this Collection 5 set of models, the percentages of various ice crystal habits are as follow: for $D_{\max} \leq 60$ μm, 100% droxtals; for $60 < D_{\max} \leq 1000$ μm, 15% 3D solid bullet rosettes, 50% solid columns, and 35% hexagonal plates; for $1000 < D_{\max} \leq 2500$ μm, 45% hollow columns, 45% solid columns, and 10% aggregates of solid columns; and for $D_{\max} > 2500$ μm, 97% 3D solid bullet rosettes and 3% aggregates of solid columns, where $D_{\max}$ is the maximum dimension of an ice particle. Baum et al. (2005, 2011) describe the development of bulk scattering models through integration over particle size distributions; the reader should refer to those studies for further details. The bulk scattering properties are averaged into a set of 18 effective diameter D_{eff} values ranging from 10 to 180 μm. The effective diameter D_{eff} is defined as

$$D_{\text{eff}} = \frac{3}{2}\frac{\int_{D_{\min}}^{D_{\max}}\left[\sum_{h=1}^{M} f_h(D)V_h(D)\right]n(D)\,dD}{\int_{D_{\min}}^{D_{\max}}\left[\sum_{h=1}^{M} f_h(D)A_h(D)\right]n(D)\,dD}, \quad (11)$$

where $D_{\min}$ and $D_{\max}$ describe the minimum and maximum particle sizes in the distribution, respectively; $f_h(D)$ is the ice particle habit fraction of habit h for size D; $n(D)$ is the number distribution for size D; and $A_h(D)$ and $V_h(D)$ are the area and volume of a specific particle of habit h for size D, respectively. The habit fraction is defined so that for each size bin,

$$\sum_{h=1}^{M} f_h(D) = 1, \quad (12)$$

each D_{eff} model includes microphysical and scattering properties such as extinction efficiency, single-scattering albedo, asymmetry factor, and scattering phase function.

Figure 4 shows examples of the phase functions (gray lines) associated with the PSDs whose effective particle sizes are within a narrow region about $D_{\text{eff}} = 50$ and 100 μm at the ABI 0.64- and 2.25-μm channels. The black curves indicate the band-averaged scattering phase functions for $D_{\text{eff}} = 50$ and 100 μm, respectively.

b. Ice particle models based on severely roughened surfaces

The second set of models of ice clouds adopted for the radiance simulator is based on a number of recent developments (Baum et al. 2011). Three new habits are now available: the hollow bullet rosette, a small aggregate of plates (five plates, each with a maximum dimension no larger than 500 μm), and a large aggregate of plates (more than five individual plates with the same size limitation). Additionally, the ice particles

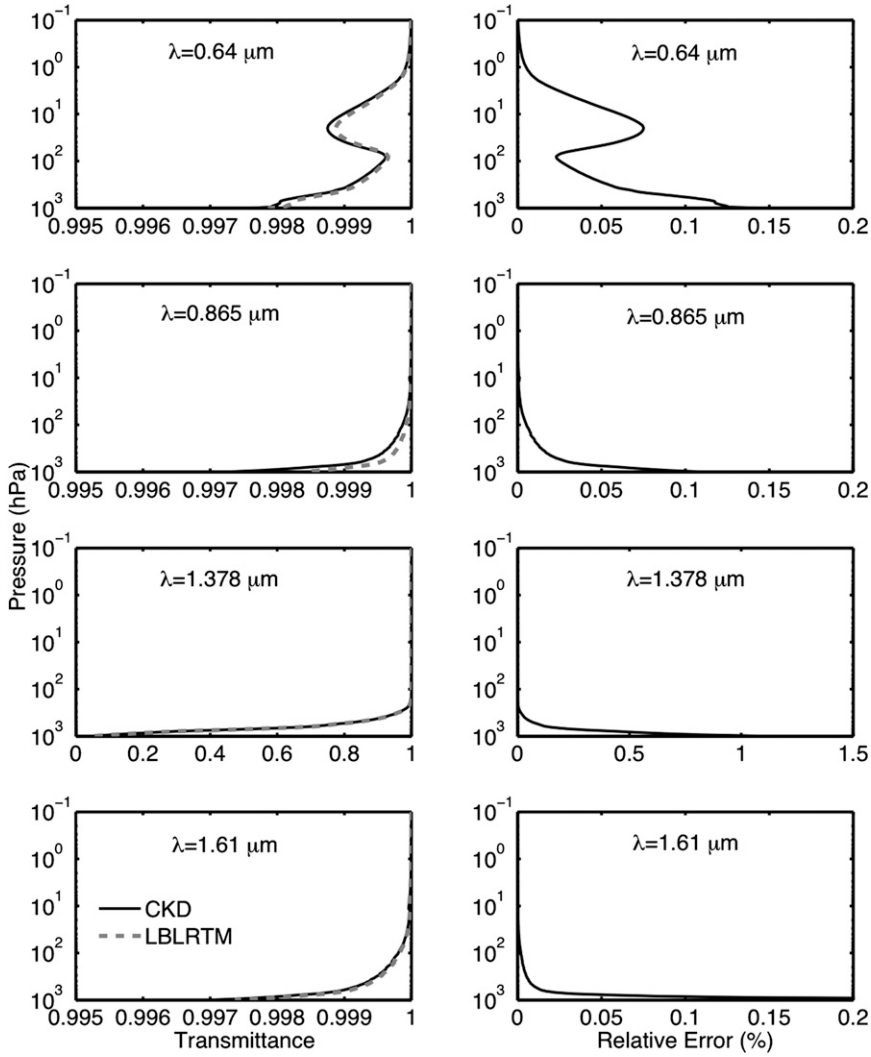

FIG. 3. (left) The band-averaged transmittance calculated from the LBLRTM and CKD models for the ABI 0.64-, 0.865-, 1.378-, and 1.61-μm channels. (right) The corresponding relative error profiles of CKD models. The tropical atmosphere profile is used in the calculations.

are assumed to be severely roughened, resulting in scattering phase functions that are smooth with no halos and significantly reduced backscattering relative to the smooth particle models. Finally, the models at small D_{eff} values are based on more physically representative particle size distributions based on improvements in in situ measurements.

4. Development of the ABI solar channel ice cloud radiance simulator

The radiance simulations at the top of the atmosphere (TOA) under cloudy-sky conditions are based on the DISORT method (Chandrasekhar 1960; Stamnes et al. 1988). DISORT is used for the calculation of the multiple scattering in a vertically inhomogeneous nonisothermal plane-parallel atmosphere, given values of the optical thickness, single-scattering albedo, and the scattering phase function for the scattering–absorbing medium in any atmospheric layer. This study is based on the publicly available and most current version of the DISORT code (DISORT 2.0 beta). DISORT requires that the phase functions be described in terms of their Legendre polynomial expansion coefficients. However, to represent the full original scattering phase function accurately, thousands of Legendre polynomial terms are needed for a phase function with the strong forward peak associated with large ice particles. To attenuate the forward

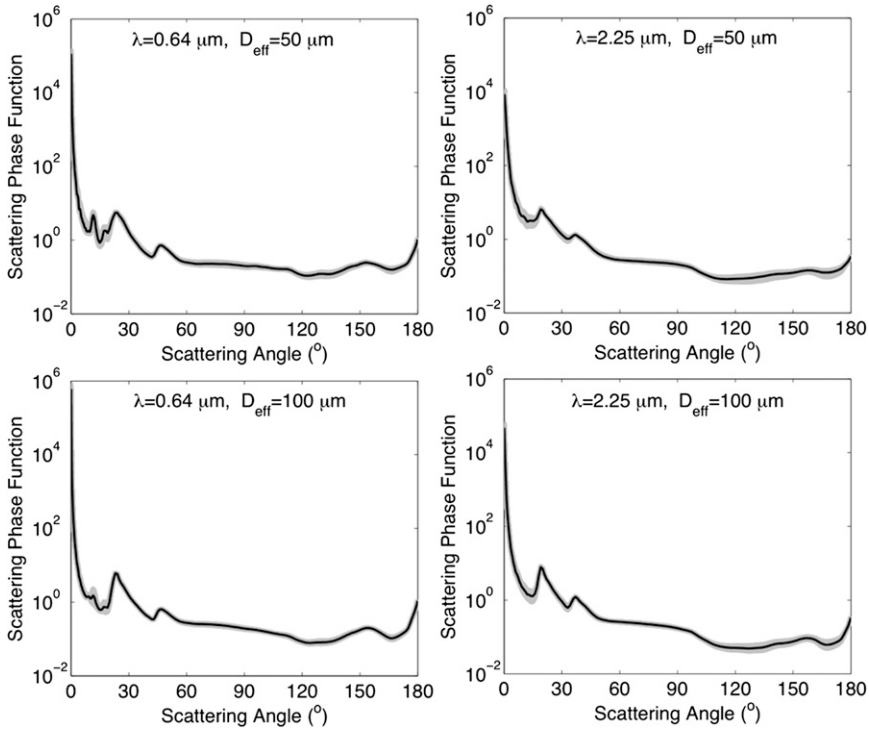

FIG. 4. The phase functions (gray lines) associated with the PSDs whose effective particle sizes fall within a narrow region around $D_{\mathrm{eff}} = 50$ and 100 μm for the ABI (left) 0.64- and (right) 2.25-μm channels. Black lines indicate the band-averaged scattering phase function at $D_{\mathrm{eff}} =$ (top) 50 and (bottom) 100 μm.

peak of the phase function of ice clouds with various effective sizes, we use the δ-fit truncation method developed by Hu et al. (2000), which in turn stems from the δ-M method (Wiscombe 1980). By truncating the forward peak and renormalizing the phase function, less than 100 terms are required to reconstruct the phase function and, thus, to decrease the computational time that is proportional to the third power of the number of radiation streams (Ding et al. 2009).

Upon truncating the forward peak, an adjustment must be made to the optical thickness and single-scattering albedo to account for the energy that was in the forward peak. Following (Liou 2002), the adjusted optical thickness and single-scattering albedo can be expressed by

$$\tau' = (1 - f\omega)\tau \quad \text{and} \tag{13}$$

$$\omega' = \frac{(1-f)\omega}{1 - f\omega}, \tag{14}$$

where f is the portion of the scattered energy associated with the truncated forward peak; τ and ω are the original optical thickness and single-scattering albedo, respectively; and τ' and ω' are the adjusted optical thickness and single-scattering albedo associated with the truncated phase function.

To simulate the radiances for the ABI, the set of CKD models described previously is used in conjunction with the DISORT model. An advantage of using the CKD method is that it can be incorporated directly into radiative transfer models to perform multiple scattering calculations for clouds and aerosol particles (Lacis and Oinas 1991). To examine the CKD+DISORT model, a set of 120 atmospheric profiles are generated by adding a small amount of random noise in the water vapor profile to a set of six standard atmospheric profiles: tropical, midlatitude summer, midlatitude winter, subarctic summer, subarctic winter, and *U.S. Standard Atmosphere, 1976*. We did not consider including variations in temperature, because our focus in this paper is on the ABI solar channels for which the temperature profiles have little effect on the upwelling TOA radiances. The LBLRTM+DISORT model combined by Ding et al. (2011) is used here to provide a reference benchmark with some minor modifications.

A single-layered ice cloud with a cloud-top altitude of 12 km and a geometrical thickness of 1 km is used for

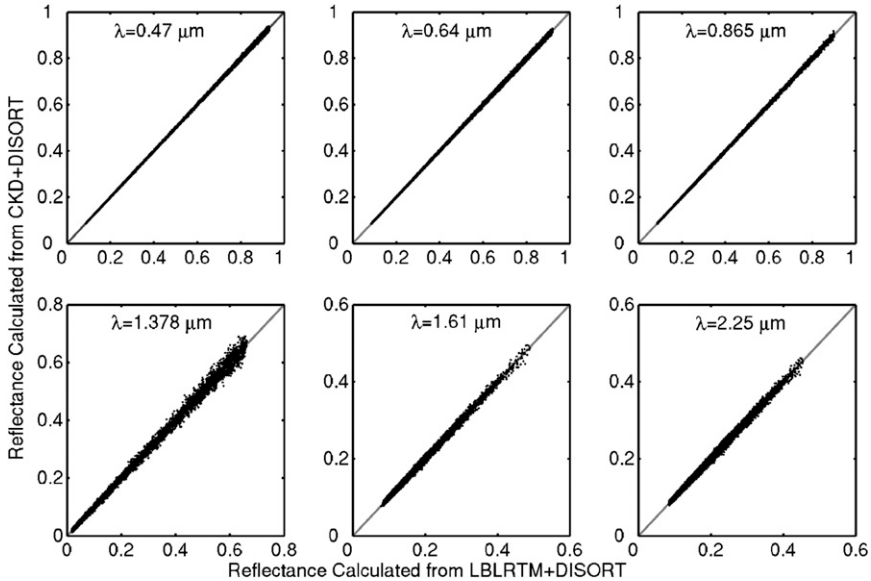

FIG. 5. Comparison of the reflectance for each ABI solar channel calculated from the CKD+DISORT (y axes) and LBLRTM+DISORT (x axes) models.

the present validation study. The ice cloud optical thickness is assumed to vary from 0 to 80 and the D_{eff} varies from 10 to 180 μm, with ice clouds having bulk scattering properties as discussed in section 3. Figure 5 shows the comparison results for the smooth particle models.

The root-mean-square (RMS) error provides an index for the overall error level of the CKD+DISORT model when compared with the LBLRTM+DISORT model. The RMS is defined by

$$\mathrm{RMS} = \sqrt{\frac{\sum_{i}^{N}(R_{\mathrm{CKD+DISORT}} - R_{\mathrm{LBLRTM+DISORT}})^2}{N}}, \tag{15}$$

where N is the total number of the simulations. The terms $R_{\mathrm{CKD+DISORT}}$ and $R_{\mathrm{LBLRTM+DISORT}}$ are used to calculate the reflectances of each model. Table 2 shows the RMS values of the ABI solar channels. The results in Fig. 5 and Table 2 indicate that radiances simulated from the CKD+DISORT model are in good agreement with those from the benchmark reference model, LBLRTM+DISORT.

5. Application

In this section, the CKD+DISORT model is used to simulate the radiances of each ABI solar channels. The simulated radiances are then compared with those of collocated MODIS level 1B products.

a. Atmospheric profiles

Since water vapor and ozone concentration profiles vary with time and location, they are treated as input parameters to the model. Other trace gases such as carbon dioxide, carbon monoxide, nitrous oxide, and methane are assumed to have constant mixing ratios in each layer. Given an atmospheric profile, the optical thicknesses related to gas absorption in each layer are calculated from the CKD models. In this study, the atmospheric profiles are provided from the MERRA products (Bosilovich et al. 2011; Rienecker et al. 2011) generated by the National Aeronautics and Space Administration Global Modeling and Assimilation Office.

TABLE 2. RMS values of the reflectances for each ABI channel from the CKD+DISORT in comparison with the LBLRTM+DISORT model.

Central wavelength of the ABI channel (μm)	0.47	0.64	0.865	1.378	1.61	2.25
RMS	0.0013	0.0014	0.0017	0.0035	0.0021	0.0023

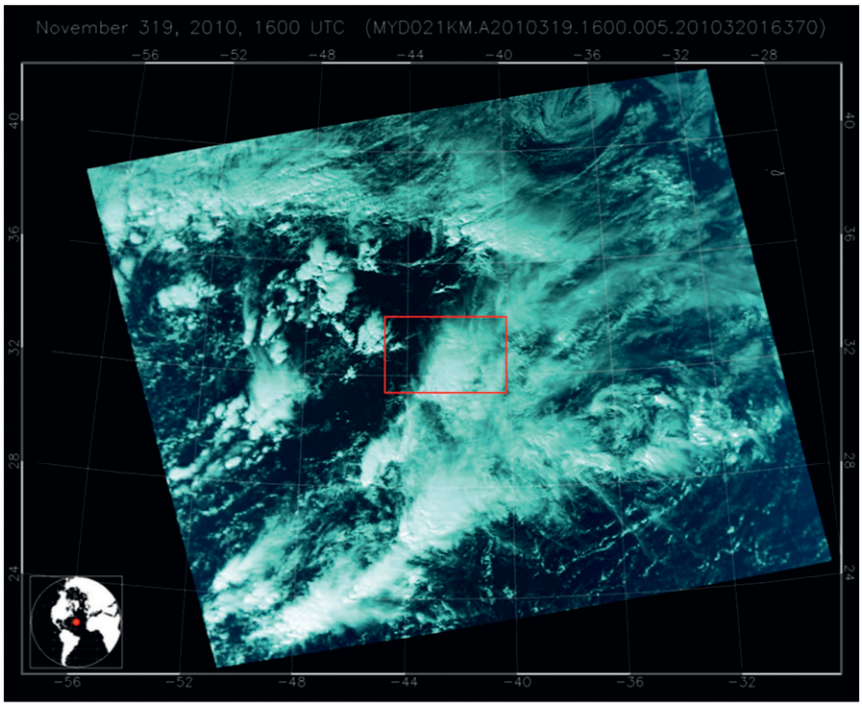

FIG. 6. MODIS visible image from the *Aqua* satellite over the Pacific Ocean on 15 Nov 2010. The red rectangle indicates the region of detailed analysis.

The profiles are employed in the CKD model to calculate the optical thickness of each layer. The 3-h vertical atmospheric profile products of MERRA (MEI3CPASM) are used in our study, which include temperature, water vapor, and ozone concentration at 42 pressure levels. The global model profiles are provided on a 288 × 144 grid with a 1.25° latitude × 1.25° longitude resolution.

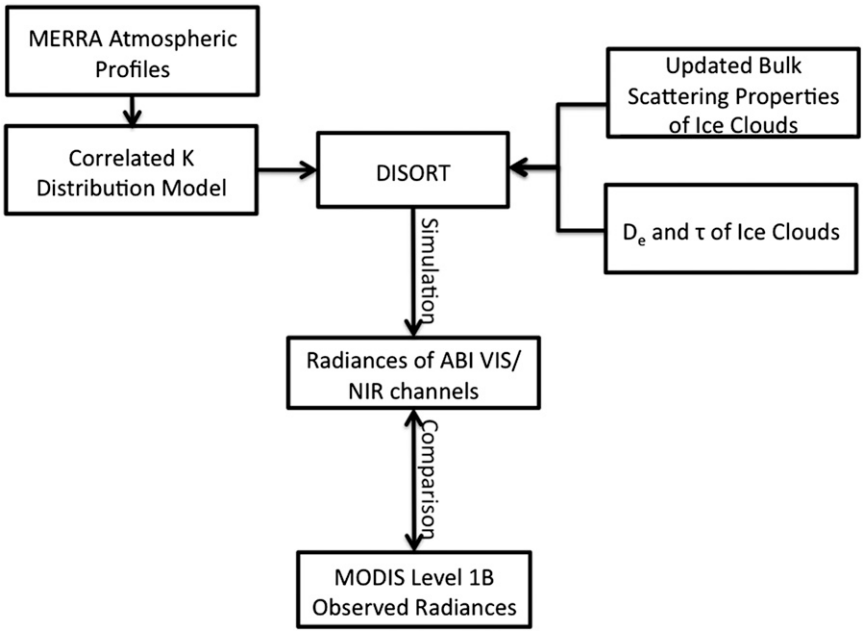

FIG. 7. Flowchart outlining the ABI solar radiance simulation using MERRA atmospheric profiles, retrieved ice cloud optical thickness, and effective particle size.

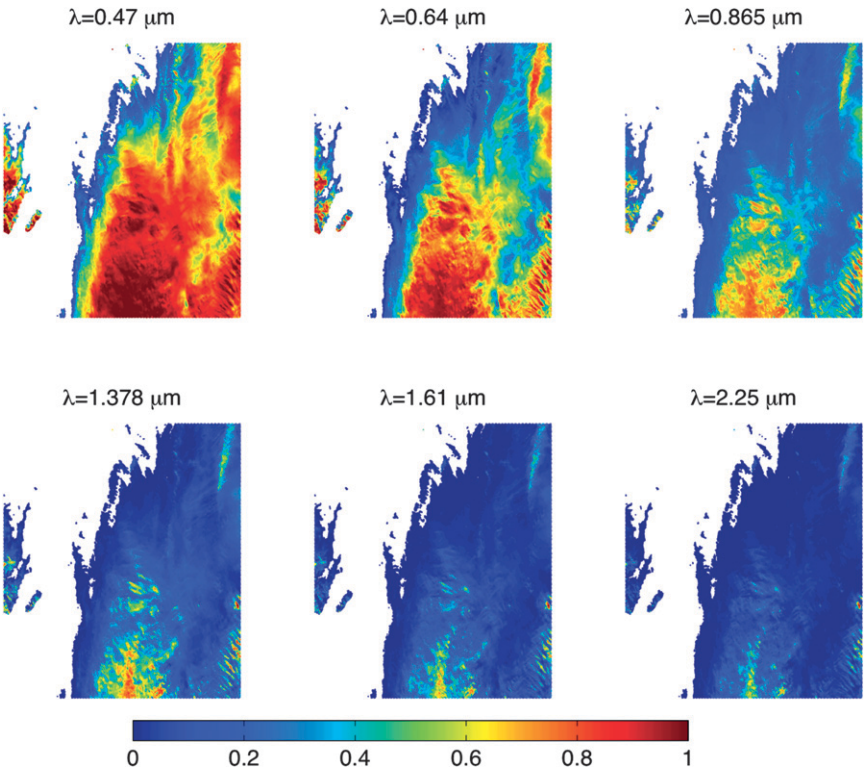

FIG. 8. Reflectances for each ABI solar channel simulated from the CKD+DISORT model. The atmospheric temperature, humidity profiles, and ozone profiles are derived from the collocated MERRA products. The ice cloud optical thickness and effective particles size are taken from MODIS Collection 5 level 2 products.

b. *Ice cloud optical thickness and effective particle size*

Two properties, the cloud optical thickness and effective particle size, are retrieved simultaneously from cloud reflectance measurements based on the bispectral reflectance technique (Nakajima and King 1990; King et al. 1992; Platnick et al. 2003) that uses one nonabsorbing band (e.g., a band centered at 0.64 or 0.865 μm) that is sensitive to cloud optical thickness and an absorbing band (e.g., a band centered at 1.61 or 2.13 μm) that is sensitive to the effective particle size. The inferred optical thickness and effective size from the MODIS observations are based on comparisons between the radiance measurements and the LUTs. For MODIS Collection 5 level 2 products, the LUTs are calculated from the bulk ice cloud scattering models based on smooth particles (Baum et al. 2005) that are described in section 3.

c. *Simulation and comparison*

In this section, the ABI solar radiances are simulated from the developed simulator and compared with MODIS measurements.

With collocated MERRA atmospheric profiles as inputs, the vertical distributions of absorption optical thickness due to the molecular absorption for each ABI solar channels associated with each weighting g are then calculated from the CKD model.

The identification of the cloud thermodynamic phase is critical for radiative transfer calculations involving clouds since the impacts of water and ice clouds on the radiative transfer in the atmosphere are significantly different. Misidentified cloud phase can give rise to significant errors in cloud radiance simulations. In this study, ice phase pixels are selected from the MODIS quality assurance (QA) 1-km data, using QA = 3 to filter out all the pixels with water, mixed, or unknown phases. Cloud-top pressures (but not cloud-top heights) are provided in the MODIS level 2 cloud product data (MYD06 Collection 5). As a note, cloud-top heights will be provided in the upcoming Collection 6 product. For this study, cloud-top heights are derived from the cloud-top pressures and the MERRA atmospheric temperature profiles. The viewing geometries of each ice cloud pixels such as solar zenith angle, solar azimuth angle, satellite viewing zenith angle, and satellite viewing azimuth angle are determined from the MODIS level 1B product.

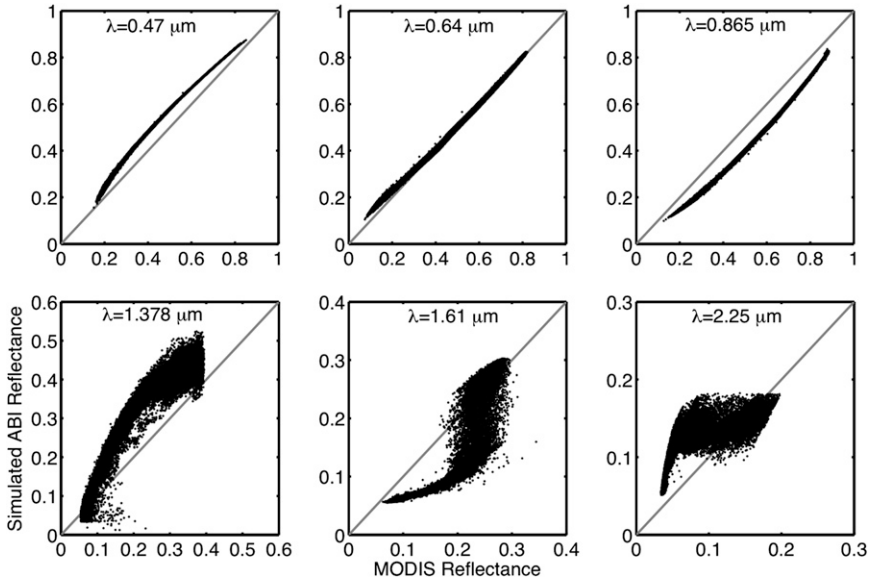

FIG. 9. Comparison of simulated reflectances of each ABI solar channel (y axes) with those from corresponding MODIS observations (x axes).

The updated band-averaged bulk scattering properties of ice clouds for the ABI solar channels are employed in the simulation. Twenty-three effective size bins from 5 to 120 μm with an increment of 5 μm are included in ice cloud scattering models of the ABI solar channels. For a given ice cloud effective particle size, the bulk scattering properties can be obtained by interpolating the ice cloud scattering models. We find that use of the logarithmic interpolation method for the derivation of the scattering phase function provides reasonably accurate results, while a linear interpolation method is sufficient for the other parameters. In addition, the derived scattering phase functions need to be renormalized (Ding et al. 2011).

To avoid larger uncertainties associated with satellite-based cloud retrievals over land, the measurements by MODIS/*Aqua* are selected over ocean. Figure 6 shows the visible image of the granule over the Pacific Ocean observed from MODIS/*Aqua* on 15 November 2010. The red outline indicates the simulation region. The ice cloud optical thickness and the effective particle size derived from MODIS level 2 products are used to represent the ice cloud optical and microphysical properties. Given the MODIS ice cloud optical thickness $\tau_{\rm vis}$ at a visible channel, the optical thickness at other channels τ_λ can be derived through the following relationship:

$$\tau_\lambda = \frac{Q_{{\rm ext},\lambda}}{Q_{\rm ext,vis}}\tau_{\rm vis}, \tag{16}$$

where $Q_{\rm ext,vis}$ is the band-averaged bulk extinction efficiency at the visible channel and $Q_{{\rm ext},\lambda}$ is the band-averaged bulk extinction efficiency at wavelength λ, both of which are from the ice cloud scattering model of ABI solar channels.

For each layer, the CKD model discussed in the previous section is employed to calculate optical thickness due to gaseous absorption. For the 0.47- and 0.64-μm channels, Rayleigh scattering is considered. Following Dutton et al. (1994) and Bodhaine et al. (1999), the atmospheric Rayleigh optical thickness is calculated approximately over the visible spectral region by

$$\tau_R = \frac{P}{P_0}0.008\,77\lambda^{-4.05}, \tag{17}$$

where p is the pressure, p_0 is 1013.25 hPa, and λ is wavelength in micrometers.

The ABI solar radiances are simulated for the focused region from the established simulator (CKD+DISORT model) given the ice cloud optical thickness and effective particle size, the collocated MERRA atmospheric profiles, and the updated ice cloud scattering model. The resulting radiance simulations are subsequently compared with those of the corresponding MODIS measurements. A flowchart outlining the current process is shown in Fig. 7.

Figure 8 shows the simulated radiances of each ABI solar channel over the region outlined by the red box in

TABLE 3. The mean imaginary index of refraction for ABI and corresponding MODIS VIS–SWIR bands.

	0.47 μm	0.65 μm	0.867 μm	1.378 μm	1.61 μm	2.25 μm
ABI	2.272×10^{-10}	1.375×10^{-8}	2.546×10^{-7}	1.575×10^{-5}	2.781×10^{-4}	2.114×10^{-4}
MODIS	1.683×10^{-10}	1.332×10^{-8}	2.093×10^{-7}	1.766×10^{-5}	2.538×10^{-4}	7.249×10^{-4}

the granule as shown in Fig. 6. It can be seen from Fig. 8 that the reflectances tend to decrease with increasing wavelength. Reflectances of ABI channels 1–3 (three nonabsorbing bands centered at 0.47, 0.64, and 0.865 μm, respectively) are significantly higher than those of the other three absorbing bands. The ABI channel 1 (0.47 μm, called the blue band) has the highest reflectance compared to the other five bands because particles scatter more at shorter wavelengths than at longer wavelengths. That is also why this band is useful for detecting aerosols and air pollution. The ABI daytime cloud property retrieval algorithms are similar to Earth Observing System MODIS. Two nonabsorbing bands (0.64 and 0.865 μm) are used with two absorbing bands (1.61 and 2.25 μm) to retrieve cloud optical thickness and the effective particle size. The 1.378-μm channel, located in a strong water vapor absorption band, will be used to detect very thin cirrus clouds and higher-level water clouds during the daytime (Gao et al. 2002) because it does not sense the lower troposphere when there is appreciable water vapor. Thus, the radiation detected by satellite at this channel is caused by scattering in the upper troposphere.

Figure 9 shows the comparison between the simulated ABI reflectances with those of MODIS level 1B products. It can be seen that the simulated reflectances of the ABI 0.47- and 0.65-μm channels are in better agreement with observed values than those of other ABI NIR and SWIR channels. To be more specific, the simulated reflectances of the ABI 0.865- and 1.61-μm channels are higher than those of the MODIS observations. However, the opposite occurs for the 1.378- and 2.25-μm channels. These differences can be explained by the following argument. The measured radiance of the satellite is the integral of the radiance weighted by the spectral response function, which can be expressed by

$$R_{\text{measured}} = \frac{\int R_\nu(\theta)\phi_\nu \, d\nu}{\int \phi_\nu \, d\nu}, \tag{18}$$

where R_ν is the radiance at the top of the atmosphere in the direction θ of the satellite. In addition, ϕ is the spectral response function. The radiances measured by two satellite instruments will differ because their spectral response functions are not the same. The upwelling radiance arriving at the satellite will be determined by the surface properties, viewing geometry, gaseous absorption in the column between the surface and the satellite, particle scattering, and absorption by clouds and aerosols. However, both the absorption coefficients of gases and the refractive index of scattering particles (ice particles in the present study) are highly spectrally dependent. Even with the same central wavelength and the same channel bandwidth, the measured radiances could still be different if both shapes of the spectral response function are not the same. Since ice clouds form mostly at very high altitudes, the amount of water vapor over these clouds is very low due to the low temperature. It can also be seen from Fig. 3 that the gaseous absorption has little effect on the transmission at high altitude. For high-level clouds, the radiances measured by a satellite depend primarily on the scattering contribution by the ice cloud particles.

The spectral refractive indices of ice are fundamental parameters that determine the relative scattering and absorption properties of cloud particles. Generally, the real part of the refractive index determines the phase speed of the electromagnetic wave, while the imaginary refractive index is related to the absorption coefficient k_λ, which is given by

$$k_\lambda = 4\pi m_i/\lambda . \tag{19}$$

A reasonable estimate of the magnitude of absorption can be made from the value of m_i. For a given narrowband spectral-response function, the mean imaginary index of refraction can be computed from (Baum et al. 2000)

$$m = \frac{\int F_s(\lambda)S(\lambda)m_i \, d\lambda}{\int F_s(\lambda)S(\lambda) \, d\lambda}, \tag{20}$$

where F_s is the spectral response function and S is the spectral solar spectrum (Kurucz et al. 1984). Table 3 shows the mean imaginary index of refraction of ABI and the corresponding MODIS solar channels.

The ABI SWIR channels are used to examine the relationship between the simulated ABI radiances and

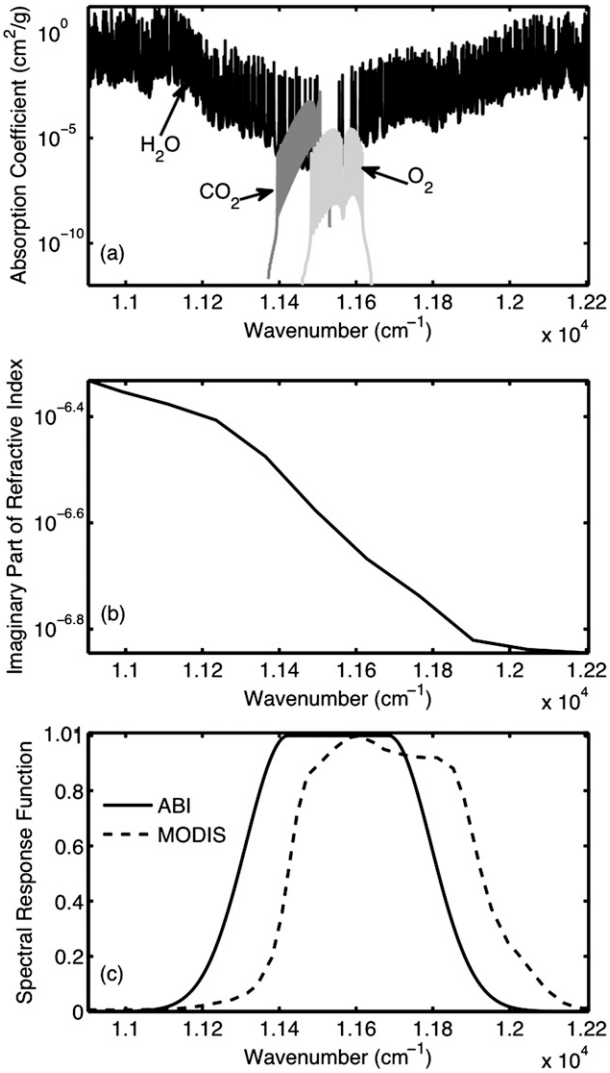

FIG. 10. (a) Absorbing gases and their absorption coefficients as a function of wavenumber over the ABI 0.865-μm channel (MODIS 0.865-μm channel) at the reference conditions of 260 K and 398 hPa. (b) The spectral imaginary part of the refractive index of ice from the compilation of Warren and Brandt (2008). (c) The spectral response functions of ABI and MODIS.

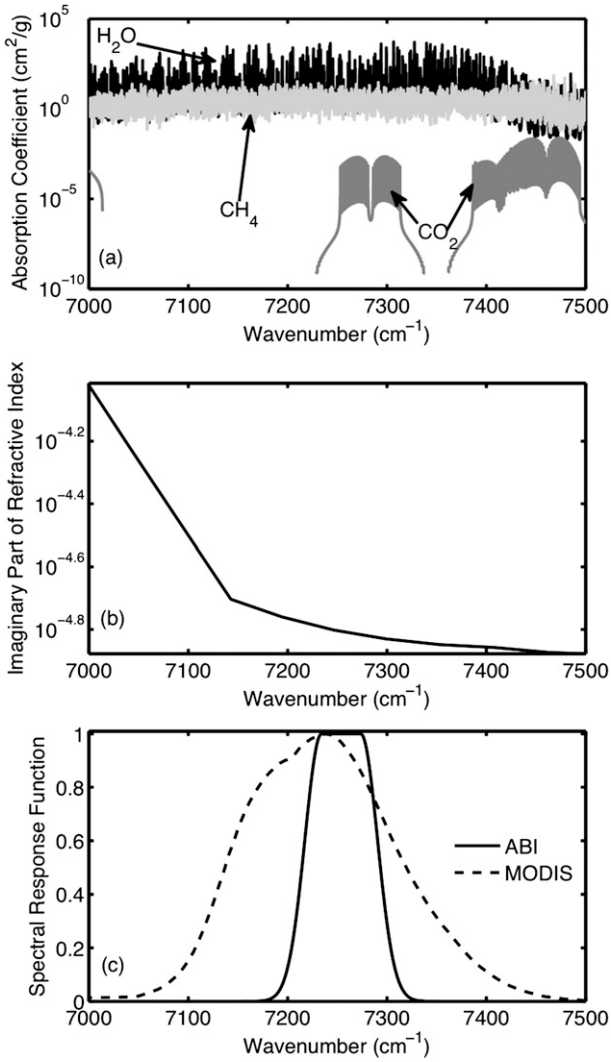

FIG. 11. As in Fig. 10, but for the ABI/MODIS 1.378-μm band.

those measured by MODIS since the mean imaginary index of refraction of ice is very small for the solar channels. The spectral response functions of MODIS and ABI, the gaseous absorption coefficients, and the refractive index of ice in the corresponding spectral regions are plotted together in Figs. 10–13. These figures show results for the four ABI SWIR channels, centered at 0.865, 1.378, 1.61, and 2.25 μm, respectively, and those from the corresponding MODIS channels. In each of these figures, panel a shows the absorption coefficients of gases in each spectral region calculated from LBLRTM model. Panel b shows the spectral imaginary part of refractive index of ice from the compilation of Warren and Brandt (2008). The spectral response functions of ABI and MODIS are shown in panel c.

For the 0.865-μm channel, the center wavelength of ABI is slightly larger than that of MODIS, and the value of the imaginary index of refraction at the ABI center wavelength of this channel is larger, as shown in Fig. 10. The mean imaginary index of refraction listed in Table 3 also shows similar results. From Fig. 9, it can be seen that the simulated reflectances of the ABI 0.865-μm channel are lower than those observed from MODIS. The same result can be seen for the 1.61-μm channel (see Figs. 12 and 9). However, for the 1.378-μm channel, the ABI has a slightly smaller central wavelength and a relatively narrower bandwidth when compared with the MODIS spectral response function (see Fig. 11). The mean imaginary index of refraction of ABI is less than that of

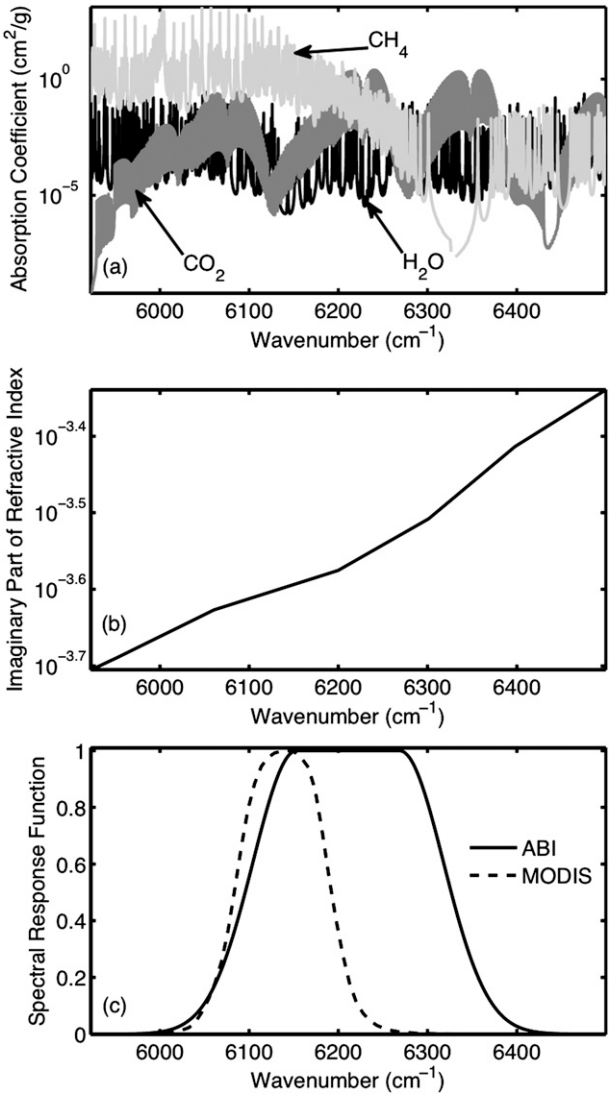

FIG. 12. As in Fig. 10, but for the ABI/MODIS 1.61-μm band.

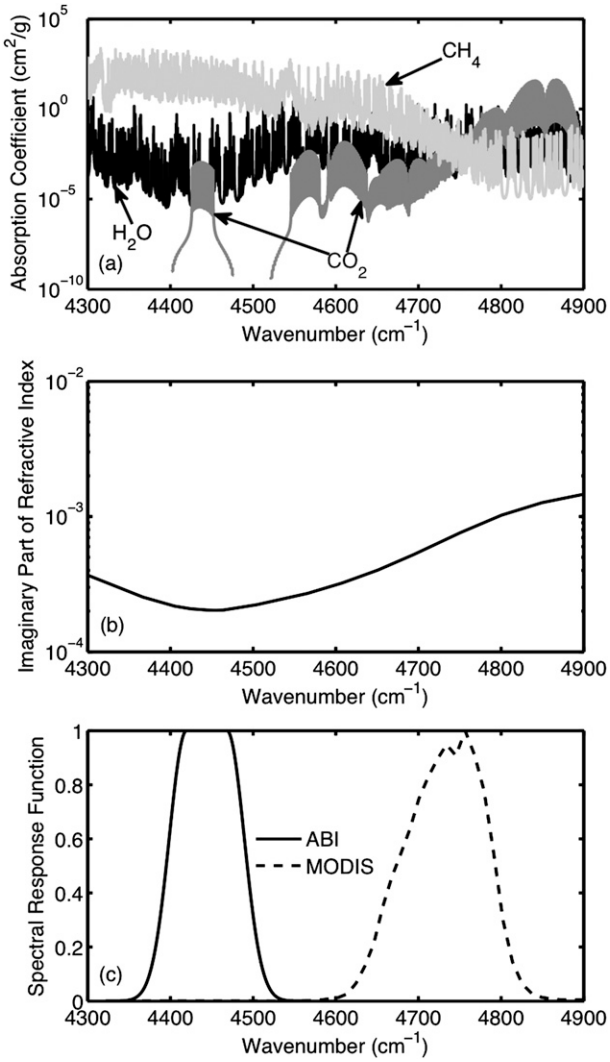

FIG. 13. As in Fig. 10, but for the ABI 2.25-μm channel (MODIS 2.13-μm channel).

MODIS. As shown in Fig. 9, the corresponding simulated reflectances of the ABI 1.378-μm channel are higher than those from MODIS for most pixels. Similar results are found for the ABI 2.25-μm channel (see Figs. 13 and 9). Thus, the differences between simulated ABI solar channel radiances–reflectances and those measured from MODIS can be explained.

Since the ice cloud properties used in the present simulation are derived from MODIS level 2 products, the differences in radiances between the ABI channels and corresponding MODIS channels might also be caused in part by errors in the MODIS effective particle size products. Further work will be needed to confirm this. In addition, in the ABI simulator, the spectral variances of transmission for the cloud-free atmosphere are considered in the CKD models, but the ice cloud optical properties are still treated as the band mean. Therefore, the treatments for gas and cloud are not consistent. Recently, Lu et al. (2011) extended the CKD method from gaseous absorption to water cloud optical properties. In future research, we will consider this approach for ice clouds.

6. Summary

In this study, we describe the development of an ice cloud radiance simulator based on the DISORT model for use with the next-generation geostationary Advanced Baseline Imager. To consider gaseous absorption in the atmosphere, a set of CKD models is developed that includes the instrument spectral response functions and

a treatment of absorption by multiple gaseous components. A subsequent comparison between the rigorous reference model and the CKD+DISORT simulator shows very close agreement.

The simulator is used to investigate the relationship between the radiances anticipated from the ABI solar channels and those measured from corresponding MODIS channels on the *Aqua* platform. To this end, the profiles of atmospheric absorption optical thickness associated with each weighting Δg are first calculated from the CKD models with collocated MERRA atmospheric profiles. With the ice cloud optical thickness and effective particle size obtained from MODIS level 2 cloud products as model inputs, the ice cloud radiances of individual ABI solar channels are simulated and compared with collocated MODIS measurements. The resulting comparisons show that there appear to be systematic differences between the simulated ABI radiances and the MODIS measurements. Further analysis indicates that the band-averaged imaginary index of refraction of ice may be the major cause leading to the radiance differences between the ABI solar channels and the corresponding MODIS channels.

Acknowledgments. This work was partially supported by a NOAA contract (EE133E-11-SE-3250) and a subcontract from the University of Wisconsin (329K453).

REFERENCES

Baum, B. A., D. P. Kratz, P. Yang, S. C. Ou, Y. X. Hu, P. F. Soulen, and S. C. Tsay, 2000: Remote sensing of cloud properties using MODIS airborne simulator imagery during SUCCESS: 1. Data and models. *J. Geophys. Res.,* **105,** 11 767–11 780.

——, P. Yang, A. J. Heymsfield, S. Platnick, M. D. King, Y. X. Hu, and S. T. Bedka, 2005: Bulk scattering properties for the remote sensing of ice clouds. Part II: Narrowband models. *J. Appl. Meteor.,* **44,** 1896–1911.

——, ——, ——, C. G. Schmitt, Y. Xie, A. Bansemer, Y.-X. Hu, and Z. Zhang, 2011: Improvements in shortwave bulk scattering and absorption models for the remote sensing of ice clouds. *J. Appl. Meteor. Climatol.,* **50,** 1037–1056.

Bodhaine, B. A., N. B. Wood, E. G. Dutton, and J. R. Slusser, 1999: On Rayleigh optical depth calculations. *J. Atmos. Oceanic Technol.,* **16,** 1854–1861.

Bosilovich, M. G., F. R. Robertson, and J. Chen, 2011: Global energy and water budgets in MERRA. *J. Climate,* **24,** 5721–5739.

Burrows, J. P., A. Richter, A. Dehn, B. Deters, S. Himmelmann, and J. Orphal, 1999: Atmospheric remote-sensing reference data from GOME—2. Temperature-dependent absorption cross sections of O_3 in the 231–794 nm range. *J. Quant. Spectrosc. Radiat. Transfer,* **61,** 509–517.

Chandrasekhar, S., 1960: *Radiative Transfer.* Dover Publications, 393 pp.

Chou, M. D., and L. Kouvaris, 1986: Monochromatic calculations of atmospheric radiative-transfer due to molecular line absorption. *J. Geophys. Res.,* **91,** 4047–4055.

Clough, S. A., M. W. Shephard, E. J. Mlawer, J. S. Delamere, M. J. Iacono, K. Cady-Pereira, S. Boukabara, and P. D. Brown, 2005: Atmospheric radiative transfer modeling: A summary of the AER codes. *J. Quant. Spectrosc. Radiat. Transfer,* **91,** 233–244.

Ding, S. G., Y. Xie, P. Yang, F. Z. Weng, Q. H. Liu, B. Baum, and Y. X. Hu, 2009: Estimates of radiation over clouds and dust aerosols: Optimized number of terms in phase function expansion. *J. Quant. Spectrosc. Radiat. Transfer,* **110,** 1190–1198.

——, P. Yang, F. Weng, Q. Liu, Y. Han, P. van Delst, J. Li, and B. Baum, 2011: Validation of the community radiative transfer model. *J. Quant. Spectrosc. Radiat. Transfer,* **112,** 1050–1064.

Dutton, E. G., P. Reddy, S. Ryan, and J. J. Deluisi, 1994: Features and effects of aerosol optical depth observed at Mauna Loa, Hawaii: 1982–1992. *J. Geophys. Res.,* **99,** 8295–8306.

Edwards, D. P., and G. L. Francis, 2000: Improvements to the correlated-*k* radiative transfer method: Application to satellite infrared sounding. *J. Geophys. Res.,* **105,** 18 135–18 156.

Fu, Q., and K. N. Liou, 1992: On the correlated *k*-distribution method for radiative transfer in nonhomogeneous atmospheres. *J. Atmos. Sci.,* **49,** 2139–2156.

Gao, B. C., P. Yang, W. Han, R. R. Li, and W. J. Wiscombe, 2002: An algorithm using visible and 1.38-μm channels to retrieve cirrus cloud reflectances from aircraft and satellite data. *IEEE Trans. Geosci. Remote Sens.,* **40,** 1659–1668.

Goody, R. M., and Y. L. Yung, 1989: *Atmospheric Radiation Theoretical Basis.* 2nd ed. Oxford University Press, 519 pp.

Greenwald, T. J., and C. J. Drummond, 1999: Computing the atmospheric absorption for the DMSP operational linescan system infrared channel. *J. Atmos. Oceanic Technol.,* **16,** 1958–1966.

Hu, Y. X., B. Wielicki, B. Lin, G. Gibson, S. C. Tsay, K. Stamnes, and T. Wong, 2000: Delta-Fit: A fast and accurate treatment of particle scattering phase functions with weighted singular-value decomposition least-squares fitting. *J. Quant. Spectrosc. Radiat. Transfer,* **65,** 681–690.

King, M. D., Y. J. Kaufman, W. P. Menzel, and D. Tanre, 1992: Remote-sensing of cloud, aerosol, and water-vapor properties from the Moderate Resolution Imaging Spectrometer (MODIS). *IEEE Trans. Geosci. Remote Sens.,* **30,** 2–27.

Kratz, D. P., 1995: The correlated kappa-distribution technique as applied to the AVHRR channels. *J. Quant. Spectrosc. Radiat. Transfer,* **53,** 501–517.

——, and F. G. Rose, 1999: Accounting for molecular absorption within the spectral range of the CERES window channel. *J. Quant. Spectrosc. Radiat. Transfer,* **61,** 83–95.

Kurucz, R. L., I. Furenlid, J. Brault, and L. Testerman, 1984: *Solar Flux Atlas from 296 to 1300 nm.* National Solar Observatory, 239 pp.

Lacis, A. A., and V. Oinas, 1991: A description of the correlated kappa-distribution method for modeling nongray gaseous absorption, thermal emission, and multiple-scattering in vertically inhomogeneous atmospheres. *J. Geophys. Res.,* **96,** 9027–9063.

Li, J., and H. W. Barker, 2005: A radiation algorithm with correlated-*k* distribution. Part I: Local thermal equilibrium. *J. Atmos. Sci.,* **62,** 286–309.

Liou, K.-N., 2002: *An Introduction to Atmospheric Radiation.* 2nd ed. Academic Press, 583 pp.

Lu, P., H. Zhang, and J. Li, 2011: Correlated *k*-distribution treatment of cloud optical properties and related radiative impact. *J. Atmos. Sci.,* **68,** 2671–2688.

Nakajima, T., and M. D. King, 1990: Determination of the optical thickness and effective particle radius of clouds from reflected

solar radiation measurements. Part I: Theory. *J. Atmos. Sci.,* **47,** 1878–1893.

Orphal, J., 2003: A critical review of the absorption cross-sections of O_3 and NO_2 in the ultraviolet and visible. *J. Photochem. Photobiol.,* **157A,** 185–209.

Platnick, S., M. D. King, S. A. Ackerman, W. P. Menzel, B. A. Baum, J. C. Riedi, and R. A. Frey, 2003: The MODIS cloud products: Algorithms and examples from *Terra*. *IEEE Trans. Geosci. Remote Sens.,* **41,** 459–473.

Rienecker, M. M., and Coauthors, 2011: MERRA: NASA's Modern-Era Retrospective Analysis for Research and Applications. *J. Climate,* **24,** 3624–3648.

Rothman, L. S., and Coauthors, 2009: The *HITRAN* 2008 molecular spectroscopic database. *J. Quant. Spectrosc. Radiat. Transfer,* **110,** 533–572.

Schmit, T. J., M. M. Gunshor, W. P. Menzel, J. J. Gurka, J. Li, and A. S. Bachmeier, 2005: Introducing the next-generation Advanced Baseline Imager on GOES-R. *Bull. Amer. Meteor. Soc.,* **86,** 1079–1096.

Shi, G., 1984: Effect of atmospheric overlapping bands and their treatment on the calculation of thermal radiation. *Chin. Adv. Atmos. Sci.,* **1,** 246–255.

——, N. Xu, B. A. Wang, T. Dai, and J. Q. Zhao, 2009: An improved treatment of overlapping absorption bands based on the correlated *k* distribution model for thermal infrared radiative transfer calculations. *J. Quant. Spectrosc. Radiat. Transfer,* **110,** 435–451.

Solomon, S., D. Qin, M. Manning, Z. Chen, M. Marquis, K. Averyt, M. M. B. Tignor, and H. L. Miller Jr., Eds., 2007: *Climate Change 2007: The Physical Science Basis.* Cambridge University Press, 996 pp.

Stamnes, K., S. C. Tsay, W. Wiscombe, and K. Jayaweera, 1988: Numerically stable algorithm for discrete-ordinate-method radiative-transfer in multiple-scattering and emitting layered media. *Appl. Opt.,* **27,** 2502–2509.

Warren, S. G., and R. E. Brandt, 2008: Optical constants of ice from the ultraviolet to the microwave: A revised compilation. *J. Geophys. Res.,* **113,** D14220, doi:10.1029/2007JD009744.

Wiscombe, W. J., 1980: Improved Mie scattering algorithms. *Appl. Opt.,* **19,** 1505–1509.

Zhang, H., T. Nakajima, G. Shi, T. Suzuki, and R. Imasu, 2003: An optimal approach to overlapping bands with correlated *k* distribution method and its application to radiative calculations. *J. Geophys. Res.,* **108,** 4641, doi:10.1029/2002JD003358.